https://doi.org/10.1016/j.ijheatmasstransfer.2019.07.037

Shedding of a condensing droplet from beetle-inspired bumps

Shakeel Ahmad, Hui Tang*, Haimin Yao

Department of Mechanical Engineering, The Hong Kong Polytechnic University, Kowloon, Hong Kong SAR, China

*Corresponding author. Email: h.tang@polyu.edu.hk

Abstract

Inspired by Namib desert beetle's bumpy structures, condensing droplet shedding from various super-hydrophobic bumps with a hydrophilic patch present on their top was numerically studied using the lattice Boltzmann method (LBM). The droplet grows on the top patch due to condensation and then sheds from the bump due to gravity. A parametric study has been conducted. It was revealed that the bump shape, diameter, height, inclination and wettability all affect the shedding volume (volume at which the droplet sheds from the bump) of the droplet. The shedding volume decreases with the bump height till a threshold height, defined as the critical bump height, beyond which the shedding volume does not change any more. With the same patch area, the shedding volume is smaller on the bump with a hemispherical top compared to the bump with a circular cylindrical top. The shedding volume increases with bump diameter, but decreases with the patch contact angle and surface inclination angle. The same trends were also found for the critical bump height. Furthermore, compared to milli-scale bumps, droplet removal followed by shedding on micro-scale bumps was found to be inefficient. Based on the simulation results, a scaling law was obtained by data fitting to estimate the critical bump height for bumps with a cylindrical top, which can be used to guide the design of desert-beetle-inspired bumps for efficient water collection from fog.

Keywords: Hydrophilic/super-hydrophobic bump; Droplet shedding volume; Critical bump height; Lattice Boltzmann method.

1. Introduction

Fresh water shortage has become a major problem in arid environments. Despite being abundant resource, only 0.36% fresh water is available for human [1,2]. The problem is more severe in arid and semiarid tropical climates, which has triggered the search for alternative sources of fresh water. Harvesting fresh water present in the form of fog can serve as a solution to this issue. In fog harvesting applications, small airborne fog droplets move along with wind, hit on mesh, coalesce into larger droplets, and get removed with the help of gravity [3]. The Namib Desert Stenocara beetles live in a desolate area and survive by drinking fog-water collected on their body shells. The Stenocara beetle's back contains many bumps with hydrophilic peaks surrounded by hydrophobic areas, which are of size about 0.5 mm in diameter with random separation of about 0.5 – 1.5 mm from each other [4]. Recently, it was found that water collection rates of beetle inspired hydrophilic/super-hydrophobic patterned surfaces were higher than that of completely hydrophilic or hydrophobic surfaces [5–8] making them potential candidate for efficient fog harvesting [3,9,10].

Efficient water collection is related to faster growth and effective removal of droplets from the surface. For this several studies have revealed the physics of droplet wetting/de-wetting mechanisms from beetle inspired surfaces. Hong et al. [11] studied pinning and de-wetting mechanism of a droplet from a designed patch on a super-hydrophobic background surface. They investigated the influence of patch shape and size experimentally, theoretically and numerically, and found that the critical surface inclination angle at which the pinned droplet de-wets the patch increases linearly with pinning length (length of pinned segment). Dorrer and Rühe [12] prepared hydrophilic/super-hydrophobic samples to mimic Stenocara beetle pattern, and investigated the droplet shedding volumes under various wettability contrasts, patch diameters and surface inclinations. Garrod et al. [13] studied micro-condensation efficiency of micro-condensers produced by fabrication of hydrophilic pixels onto super-hydrophobic background. They investigated chemical nature and dimensions of hydrophilic pixels and obtained optimum hydrophilic pixel size to center-to-center distance ratio (500 μm / 1000 μm) by comparing condensation results with Stenocara beetle's elytra pattern.

Fog harvesting is an extremely complex process in which droplet grows by coalescence of successively impacting droplets on surface and its subsequent gravitational shedding may also by influenced by air drag force. In the present work, a relatively simple approach of fog droplet condensation from pure vapor is adopted with focus placed on the roles of surface wettability and topographical characteristics on droplet shedding dynamics. Though the approach is simple, the outcome of this work can provide an insight for novel design of efficient fog harvesting surfaces.

Furthermore, in above studies droplet shedding from patched hydrophilic/hydrophobic surfaces for different patch shapes and wettability contrasts was mainly discussed, while the convex topography and height of beetle's bump were given less attention. This motivated us to study the roles of curvature and height of beetle-inspired bumps on the shedding dynamics of condensing droplets, in which the effects of various bump parameters, including bump shape, size, height, inclination and wettability will be studied.

2. Problem definition

Figure 1 shows the schematic and computational domain of the problem. A seed droplet is initially placed on a bump of diameter d and height h. Water vapor enters the domain from the top side with a constant velocity. The seed droplet grows by condensation, slides downward due to the gravity, and eventually sheds from the bump. In this study, the volume at which the droplet sheds from the bump is defined as the shedding volume (V_s).

To study the effect of bump shape on the droplet shedding volume, three types of bumps are selected, i.e., one cylindrical (Fig. 2(a), denoted as C bump) and two hemispherical (Figs. 2(b) and 2(c), denoted as H1 bump and H2 bump, respectively). The central hydrophilic patch and surrounding super-hydrophobic areas are colored in green and gray, respectively, as shown in Fig. 2. For the C bump, the diameter of the hydrophilic patch on the top of bump is d. For the H1 and H2 bumps, the top hemisphere has a diameter of d. For the H1 bump, the height of the hydrophilic patch is set as $h_p = d/4$, such that its area is the same as in Case C. With this setting, the effect of surface curvature on droplet shedding can be studied. For the H2 bump, the hydrophilic patch occupies the entire hemisphere, and hence has an area twice the area for the C and H1 bumps.

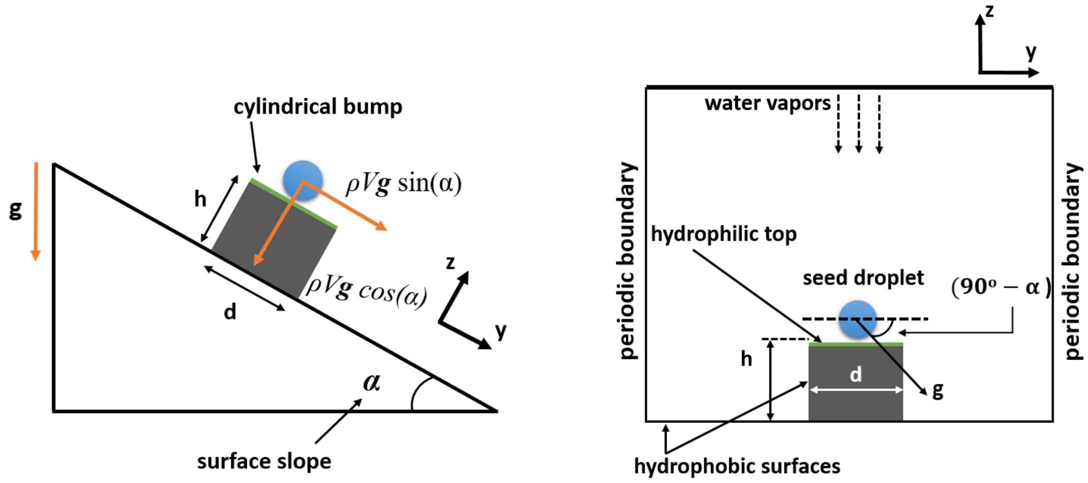

(a) (b)

Fig. 1. (a) Schematic and (b) computational domain of the problem.

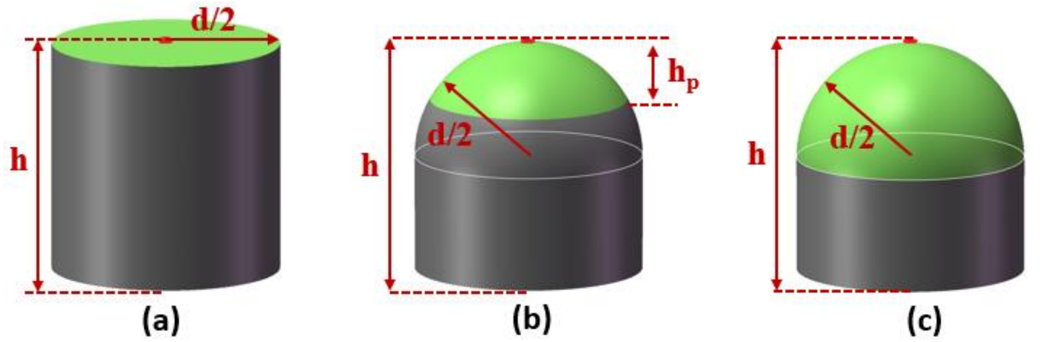

Fig. 2. (a) Cylindrical (C) bump with a hydrophilic patch on its top; (b) Hemispherical (H1) bump with a hydrophilic patch having the same area as on the cylindrical bump; and (c) Hemispherical (H2) bump with a hydrophilic patch having an area twice as on the cylindrical bump. The hydrophilic patch areas are in green while the surrounding super-hydrophobic areas are in grey.

The parameters involved in this problem are as follows (see Figure 1): the surface inclination angle α, the surrounding gas density ρ_g and viscosity μ_g, the liquid droplet diameter D, droplet density ρ, viscosity μ, surface tension σ, gravitational acceleration

$\boldsymbol{g}$, contact angle of hydrophilic patch θ_{patch} and contact angle of super-hydrophobic area θ, bump height h and bump diameter d.

To make the study more focused, some of the above parameters are fixed in the present study. Due to the numerical stability issues at high density ratios, in the present LBM simulations the liquid-to-gas density ratio is fixed at ρ/ρ_g = 114.5. Following Dorrer and Rühe [12], the contact angle of super-hydrophobic surface is fixed at 176°.

The lattice unit value of gravity is determined from the Bond number Bo that describes the ratio of gravitational force to surface tension force.

$$\mathrm{Bo}=\Delta\rho \boldsymbol{g} D^2/\sigma \tag{1}$$

where D is spherical equivalent diameter of droplet. Simulation are conducted with different length unit conversion factors. These conversion factors lead to different lattice unit values of gravity for the same physical gravitational acceleration $\boldsymbol{g}$ = 9.8 m/s^2 as shown Table 1. In LBM lu and tu denote length unit and time step, respectively. For larger conversion factors the shedding droplet size in lattice units is small, e.g., D = 36.1 for 1 lu = 100 um, which does not contain enough lattice points to fully resolve the gravitational pull and hence comes with large errors. The conversion factor 1 lu = 50 um with $\boldsymbol{g}$ = 1.53×10^{-5} lu/ts^2 has a relative error less than 1% and hence was chosen in this work.

Table 1. Effect of lattice to physical unit conversion factor and gravity on shedding droplet size

Lattice to physical unit conversion factor	1 lu= 20 um	1 lu= 25 um	1 lu= 50 um	1 lu= 100 um
Gravity in lattice unit (lu/tu^2)	2.46×10^{-6}	3.84×10^{-6}	1.53×10^{-5}	6.16×10^{-5}
Shedding droplet diameter (lu/mm)	157/3.14	127/3.17	63.5/3.17	36.1/3.61
Relative error (%)	--	0.95	0.95	14.96

Time can be converted to physical time by dimensionless time given as

$$t^*=t(\boldsymbol{g}/d)^{1/2} \quad (2)$$

Inlet vapor velocity can also influence the droplet shedding volume due to condensation rate change. Simulations were conducted for different inlet velocities (see Table 2). The velocity V_{inlet} = 0.008 lu/ts was finally selected, as it has a relative error smaller than 1% and shedding time in lattice unit significantly shorter than the other smaller velocities making it computationally inexpensive.

Table 2. Effects of inlet velocity on shedding droplet size

V_{inlet} (lu/ts)	0.004	0.006	0.008	0.01	0.015
Shedding droplet diameter (lu/mm)	63.05/3.15	63.20/3.16	63.5/3.17	65.0/3.25	67.6/3.38
Relative error (%)	--	0.31	0.63	3.17	7.30
Shedding time (tu)	40000	36000	26100	22200	16820

3. Methodology

The LBM has achieved considerable success as an alternative approach of simulating multiphase flow problems [14]. The fundamental procedure of LBM is to solve the kinetic equation for the particle distribution function [15]. The macroscopic variables, such as velocity and density, are determined from the moments of these distribution functions. The LBM due to its kinetic nature has many advantages, such as simple boundary conditions and natural adoption of parallelization.

In this study, the three-dimensional pseudopotential LBM is used to simulate the condensation on selected bumps. This method is based on the Shan-Chen scheme [16,17] in which the phase segregation is achieved by interparticle interaction force. The Carnahan-Starling equation of state is employed for better stability at larger density ratios. An in-house C++ code was used for the simulations. Further mathematical formulations and implementation of this method can be found in [18]. The wetting characteristics of the surface are achieved by computing a specific adhesion force between the gas/liquid phase and solid walls as explained by Benzi et al. [19]. In the past, the LBM has been successfully used for condensation related problems [20,21]. Dupuis and Yeomans [22] employed LBM to investigate droplet condensation on Beetle inspired bumps and found that chemical patterning on the beetle's back is important for water droplet formation. Zhang et al. [21] used a multicomponent LBM based on the Shan-Chen scheme to simulate dropwise condensation on nano-structured surfaces. Fu et al. [23] employed the pseudopotential LBM to simulate condensation on structured surface to investigate preferential nucleation modes of condensate droplets.

The present LBM framework is validated by the Laplace law test in which the pressure difference across a droplet interface ΔP is related to the surface tension σ as follows

$$\Delta P = \sigma / R \tag{3}$$

where R is the droplet radius. A droplet is equilibrated in a periodic domain of lattice nodes 140 × 140 × 140, and pressure difference is plotted against inverse of droplet radius in Fig. 3, which shows a good agreement with an average error of 0.9% between the simulation and analytical results.

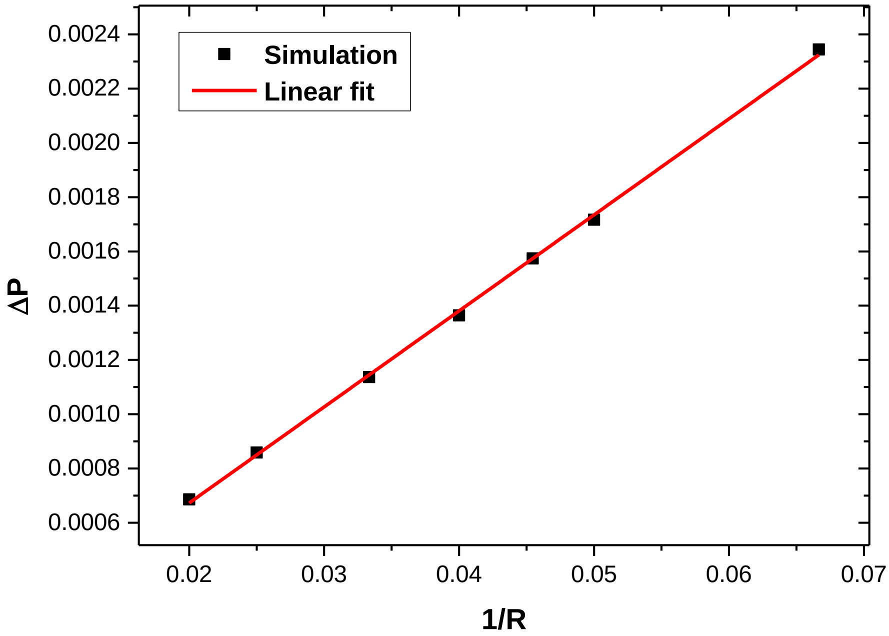

Fig. 3. Laplace law validation.

The LBM framework is then validated for droplet shedding from a circular patch on a tilted surface. Consider a droplet on a hydrophilic patch in a tilted super-hydrophobic surface. The droplet would roll off the surface once its volume reaches the shedding volume. The criterion for droplet to remain attached to surface is that the pinning force must be equal to or greater than the gravitational pulling force exerted on the droplet [24,25]. Dorrer and Rühe [12] modified the expression of droplet shedding volume as

$$V_s = \lambda_{CL}^2 \, d \, (\cos \theta_{patch} - \cos \theta) \tag{4}$$

where d is the diameter of patch representing the width of the solid-liquid contact. Note that this equation is only applicable to a circular patch in a super-hydrophobic background surface. The angles θ_{patch} and θ are equilibrium contact angles representing the receding contact angle on the patch and advancing contact on the super-hydrophobic background surface, respectively. To simplify the problem, the contact angle hysteresis on patch and super-hydrophobic surfaces is not taken into account.

λ_{CL} in Equation (4) is the modified capillary length, which is evaluated by incorporating the gravity effect through the surface inclination α

$$\lambda_{CL} = (\sigma / \rho g \sin \alpha)^{1/2} \quad (5)$$

Simulations are conducted with two surface inclinations, i.e., α = 18° and 32°, and three different patch wettability, i.e., θ_{patch} = 23°, 81° and 101°. The contact angle of the super-hydrophobic surface is kept constant at θ = 176°. The simulation results are then compared to experimental [12] and Eq. (4). Overall there is good agreement among analytical, experimental and simulation results (Fig. 4). However, at the higher wettability contrast, i.e, θ_{patch} = 23°, θ = 176° and $\cos\theta_{patch} - \cos\theta$ = 1.91, significant discrepancies appear between experimental and analytical (largest ~31%) and between experimental and simulation results (largest ~19%), which can be attributed to the droplet meniscus instability [12].

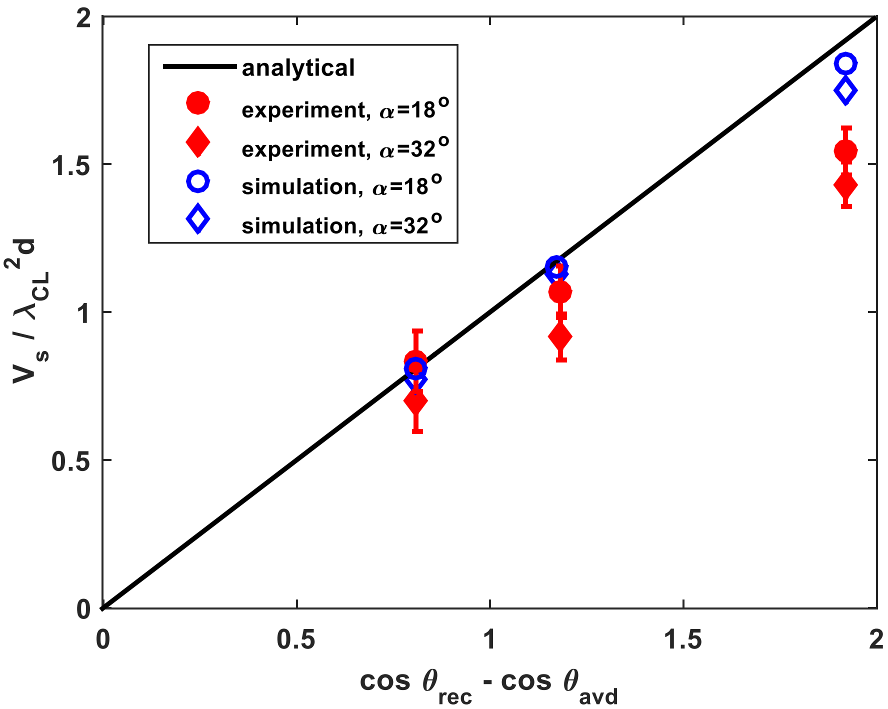

Fig.4. Normalized shedding volume versus wettability contrast.

In the present study, the computational domain is a three-dimensional rectangular box with a cylindrical or hemispherical bump located on its lower wall (Fig. 1(b)). Periodic boundary conditions are used on the left and right sides of the domain. Bounce back boundary conditions are employed on the bottom surface as well as the bump walls to implement the no-slip boundary condition. To introduce the vapor source, the velocity inlet boundary condition is applied on the top side [26,27]. Grid independence was checked for a cylindrical patch of d=2 mm. The grid with 180 (x) × 220 (y) × 220 (z) nodes has a relative error less than 1% (as listed in Table. 3). Therefore, by considering the trade-off between the accuracy and the computational cost, grid 180×220×220 was chosen.

Table 3. Grid independence test

Grid size(x y z)	Shedding volume (μl) (Patch d = 2 mm)	Relative error (%)
160×220×220	33.57	4.54
180×220×220	34.92	0.71
200×220×220	35.04	0.36
180×180×220	33.54	4.63
180×200×220	34.91	0.73
180×240×220	34.93	0.90
180×220×150	34.913	0.73
180×220×300	34.915	0.73
200×240×300	35.17	--

4. Results and discussion

4.1 Dynamics of a droplet shedding from a cylindrical bump

Figure 5 shows a droplet being dislodged from a hydrophilic circular patch on a tilted plane. Droplet growth, necking and shedding processes are captured by a time sequence of mid-span images in Fig. 6. The patch diameter, surface slope and patch contact angle are fixed at d = 2 mm, α = 45° and θ_{patch} = 50°, respectively. In the beginning, the seed droplet grows bigger by condensation till it occupies the whole patch. The gravity component parallel to surface pulls the condensing droplet downward. However, the downhill contact line remains pinned until the downhill contact angle approaches the contact angle of the super-hydrophobic region (Fig. 6(b)). When the droplet size further increases and the downhill contact line starts to move downwards, the uphill contact line remains pinned since its contact angle has not reached the contact angle of patch (Fig. 6(c)). The droplet volume further increases with time while the downhill contact line keeps moving (Figs. 6(d) and 6(e)). Because of this downhill motion of droplet, the uphill contact angle keeps reducing. Once it reaches the contact angle of patch, the uphill meniscus starts to move downwards (Fig. 6(f)). Moreover, larger gravity force due to the increased size causes necking of droplet at its uphill side. The neck elongates and ruptures even before the contact line could completely de-wets the patch, and thus leaves behind a small portion of the droplet on patch, while the remaining larger portion sheds down the patch (Figs. 6(g) and 6(h)).

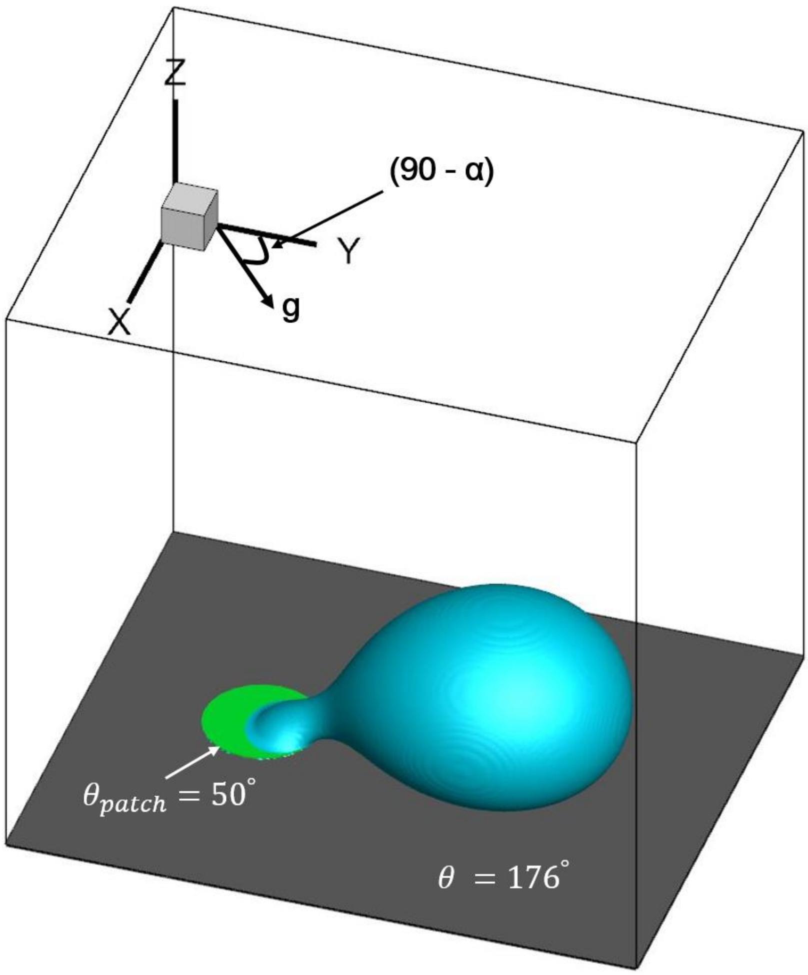

Fig.5. Droplet shedding from a circular hydrophilic patch at time *t* = 58000, where *d* = 2 mm, *α* = 45° and *θ*$_{patch}$ = 50°.

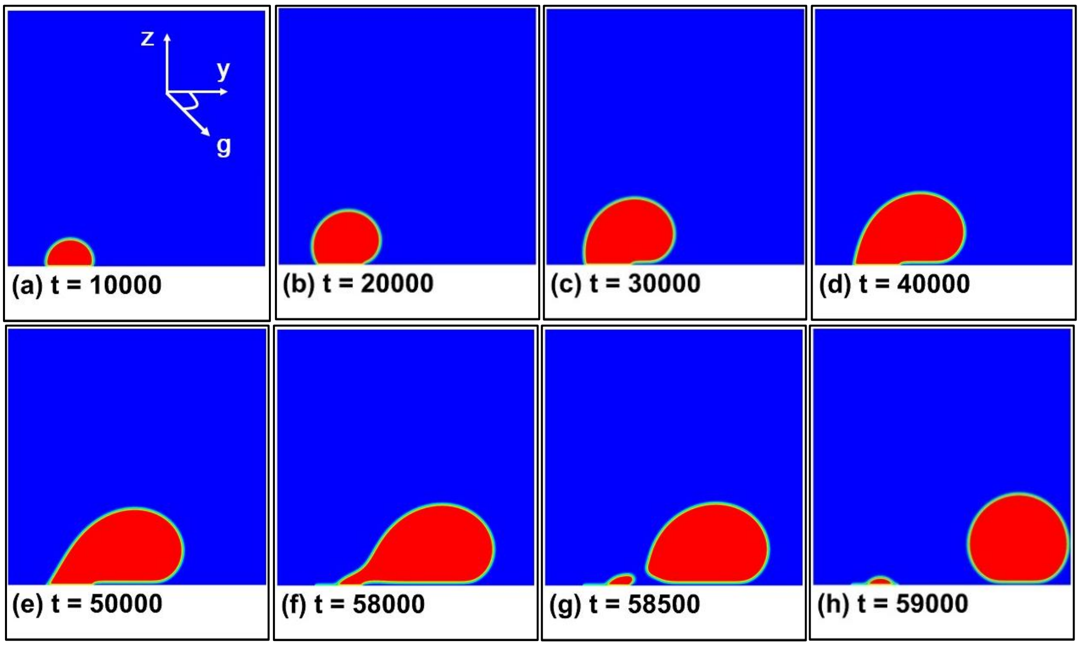

Fig.6. A time sequence of mid-span images showing the growth of a droplet and its rolling off from a circular hydrophilic patch.

If the circular patch extrudes in z direction to a height h = 1.5 mm, similar droplet growth can be found during the initial stage (by comparing Figs. 7 (a1) and 7 (b1)). At t = 30000 (Fig. 7(a2)), a bulge at droplet downhill side appears in the circular patch case, suggesting the movement of its front part into super-hydrophobic region. In the cylindrical bump case this front bulging part also droops downward due to the action of the z component of gravity (Fig. 7(b2)). The simultaneous action of both y and z components of gravity induces the downhill drooping motion of droplet. This drooping part in turn decreases the uphill contact angle faster than in the circular patch case. So, the droplet necking and shedding occur earlier, which also affects the droplet's shedding volume.

To further study the influence of bump height on the shedding volume, simulations are conducted for cases with different bump heights. Figure 8 shows the variation of shedding volume against the bump height. It is seen that the shedding volume is maximum at zero bump height (i.e., in the circular patch case), and decreases with increasing the bump height till a certain value, beyond which the shedding volume levels off. The bump height when the shedding volume starts to level off is hence defined as “critical bump height” h_c. In this study, h_c is determined when the shedding volume reaches a value that is 1.5% higher than its level-off value, as depicted by a red vertical bar in Fig. 8. It is seen from Fig. 8 that h_c = 1.1 mm in this case.

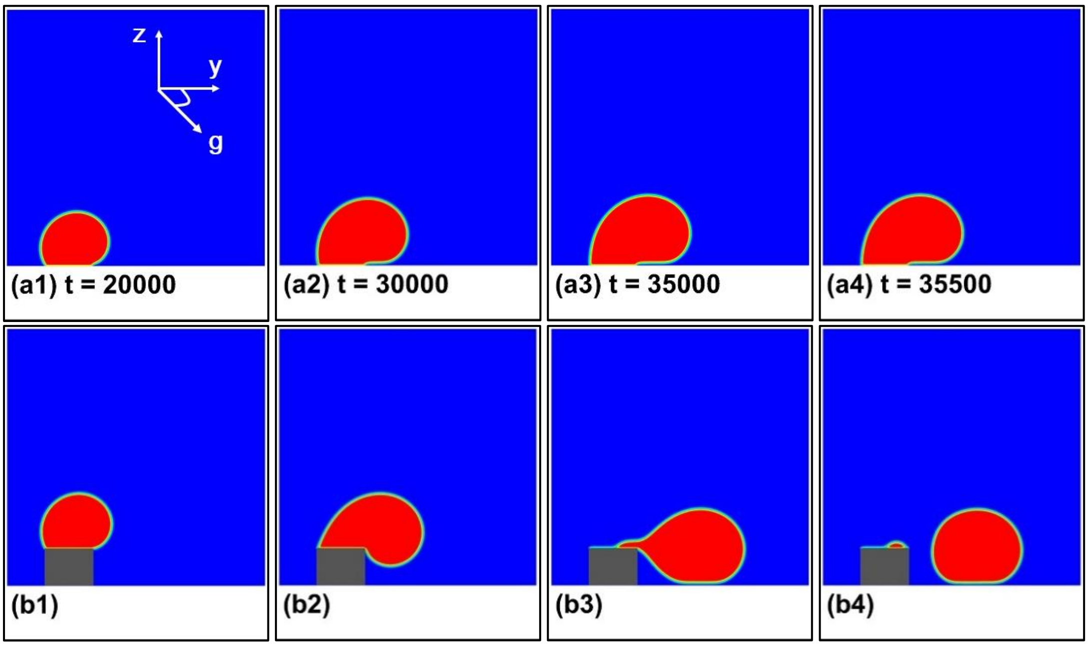

Fig.7. Time sequences of a droplet growing and shedding on (a) a circular patch (b) the C bump.

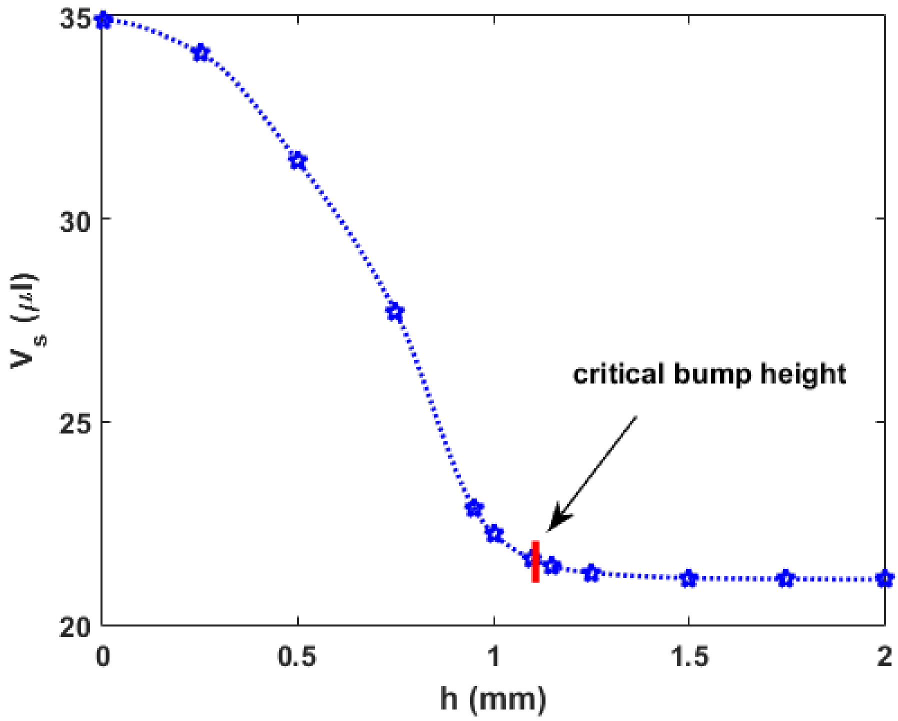

Fig.8. Variation of droplet shedding volume against bump height. The red bar indicates the critical bump height.

4.2 Effects of bump shape, diameter, inclination and patch wettability

The effects of bump shape on droplet growth and shedding are investigated with three types of bumps, i.e., C bump with a circular hydrophilic patch on its top end (Fig. 2(a)), H1 bump with an equi-area hydrophilic patch on its hemispherical top (Fig. 2(b)), and H2 bump with a twice-area hydrophilic patch on its hemispherical top (Fig. 2(c)). The bump heights in all the cases are fixed at h = 1.5 mm.

The snapshots of droplet evolution at selected instants are shown in Fig. 9. It is seen that the droplet sheds from the C bump at about t = 35500 (Fig. 9(a4)), whereas it sheds from the H1 bump much earlier at about t = 28000 due to its steeper slope caused by the curvature (Fig. 9(b4)). If the area of hydrophilic patch in the H1 bump is doubled as in the H2 bump, the droplet's downward part touches down on the surrounding hydrophobic surface earlier. However, it remains in contact with the bump for a much longer time because of its larger hydrophilic patch area (Figs. 9(c4) and 9(c5)). This significantly delays the droplet shedding time (t = 56000, see Fig.9 (c6)). On the other hand, if the height of H2 bump is increased from h = 1.5 mm to 3.5 mm, the condensing droplet can droop further to help reduce the contact area with the patch (compare Figs. 9(c3) and 9(d3)), which leads to earlier droplet shedding (Fig. 9(d4)).

As revealed in Fig. 9, at h = 1.5 mm the fastest droplet shedding occurs on the H1 bump (Fig. 9(b4)), while the slowest shedding occurs on the H2 bump (Fig. 9(c6)). Therefore, the shedding volume is smallest for the H1 bump and largest for the H2 bump, which is clearly reflected in Fig. 10. If the height of the H2 bump is increased to 3.5 mm, the shedding volume decreases as a result of reduction in shedding time. Fig. 10 also reveals that the critical bump heights h_c is 1.1 mm for the C bump, 1.5 mm for the H1 bump and 3.2 mm for the H2 bump. The C bump has the largest shedding volume at its critical height, whereas the H1 and H2 bumps have similar shedding volumes at their respective critical heights.

It is interesting to see prominent necking phenomenon on the C and H2 bumps at h = 1.5 mm (Figs. 9(a4) and 9(c5)). This is because from these two bumps droplets of relatively larger volumes can be produced, as confirmed in Fig. 10. As such, larger gravity force is acted on the droplet compared to the surface tension force, causing a more elongated necking film and a flatter droplet. The rupture of this neck then leaves behind a small amount of liquid on the hydrophilic patch, as shown in Figs. 9(a5) and 9(c6).

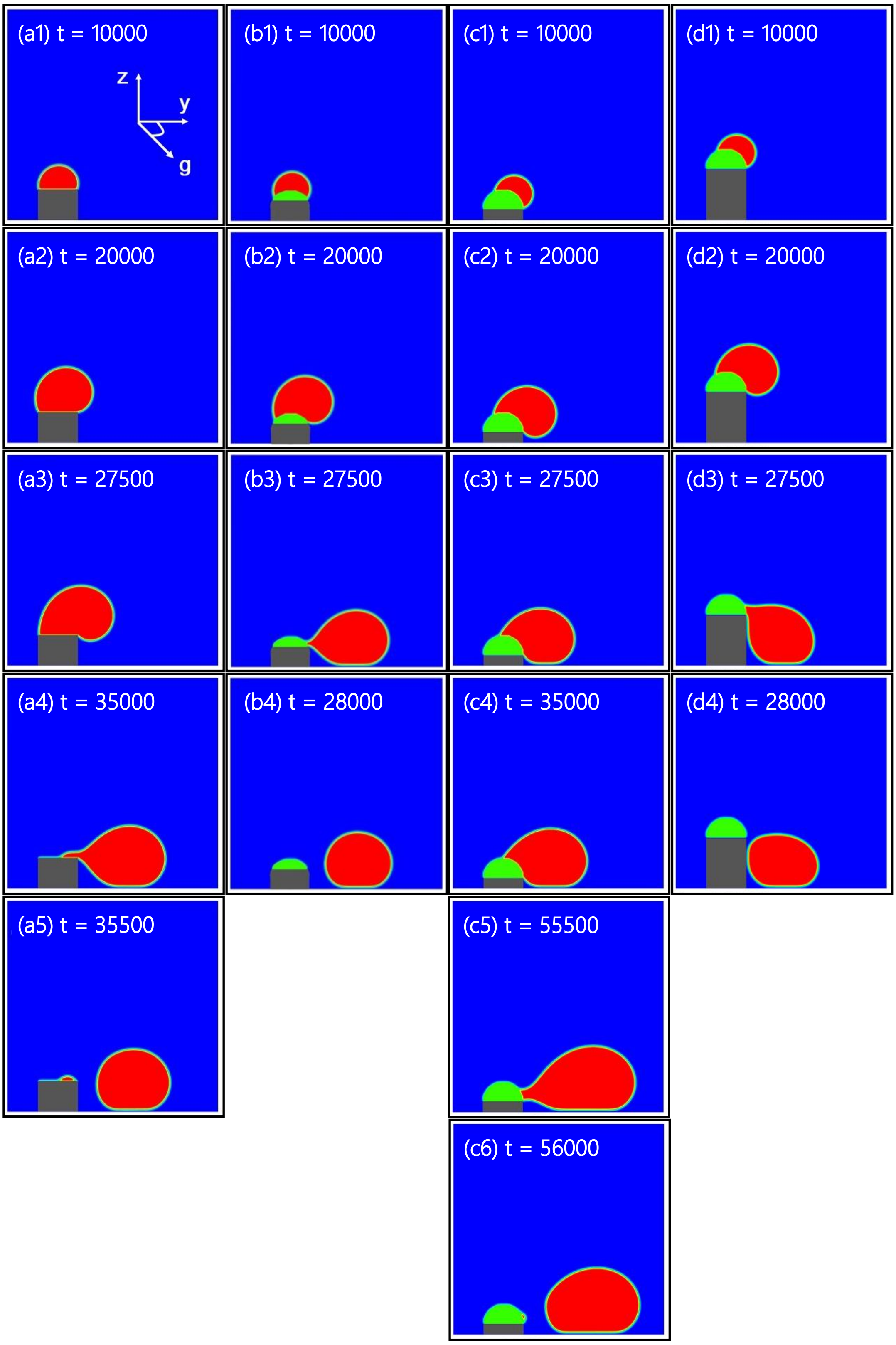

Fig.9. Droplet shedding from (a) the C bump with *h* = 1.5 mm, (b) the H1 bump with *h* = 1.5 mm, (c) the H2 bump with *h* = 1.5 mm and (d) the H2 bump with *h* = 3.5 mm.

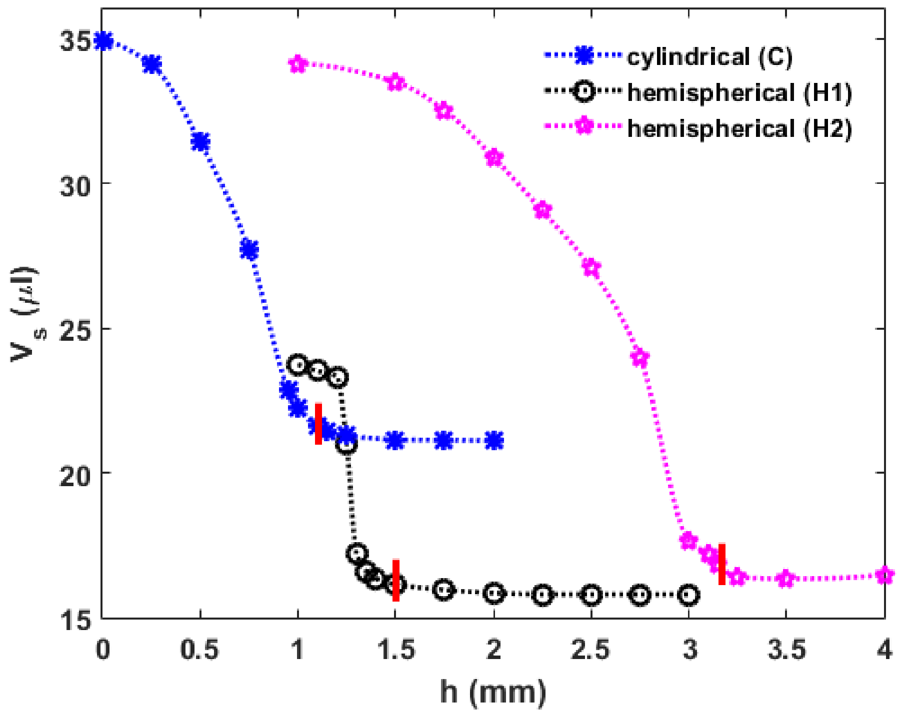

Fig.10. Variation of droplet shedding volume against bump height for different bump shapes. The red bars indicate the critical bump heights.

To study the effects of bump diameter on the critical bump height, the bump diameter is varied from d = 1 mm to 4 mm with an interval of 1 mm. Surface inclination and contact angle of the hydrophilic patch are fixed at $\alpha = 45^{o}$ and $\theta_{patch} = 50^{o}$, respectively. Increasing bump diameter increases the solid-liquid contact dimension perpendicular to direction of droplet shedding. This increases the pinning resistance force and hence a greater gravitational force is required to remove the droplet. Figure 11 shows the variation of shedding volume against the bump height for bumps of four different diameters. The trends are similar, that is, increasing bump diameter increases shedding volume. In addition, the critical bump height also increases with bump diameter.

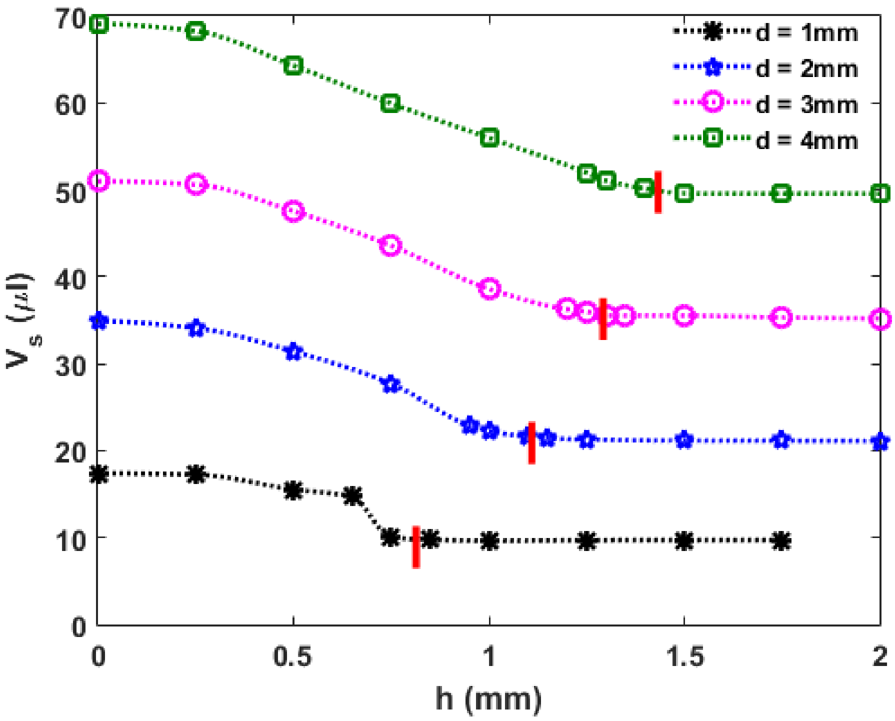

Fig.11. Variation of droplet shedding volume against bump height for different bump diameters. The red bars indicate the critical bump heights.

Surface inclination also affects the shedding volume and critical bump height of shedding droplet, as changing inclination alters the magnitudes of perpendicular and parallel gravity components. The bump diameter and patch contact angle are fixed at d = 2 mm and θ_{patch} = 50^o, respectively. The surface inclination is varied from α = 30^o to 60^o with an interval of 15^o. It is seen from Fig. 12 that generally the shedding volume reduces with the increase of surface inclination due to the reduction of the along-surface gravity component. At smaller surface inclination (e.g., α = 30^o), quite large shedding volume is found when the bump height is under its critical height. Besides, the critical bump height increases with decreasing surface inclination.

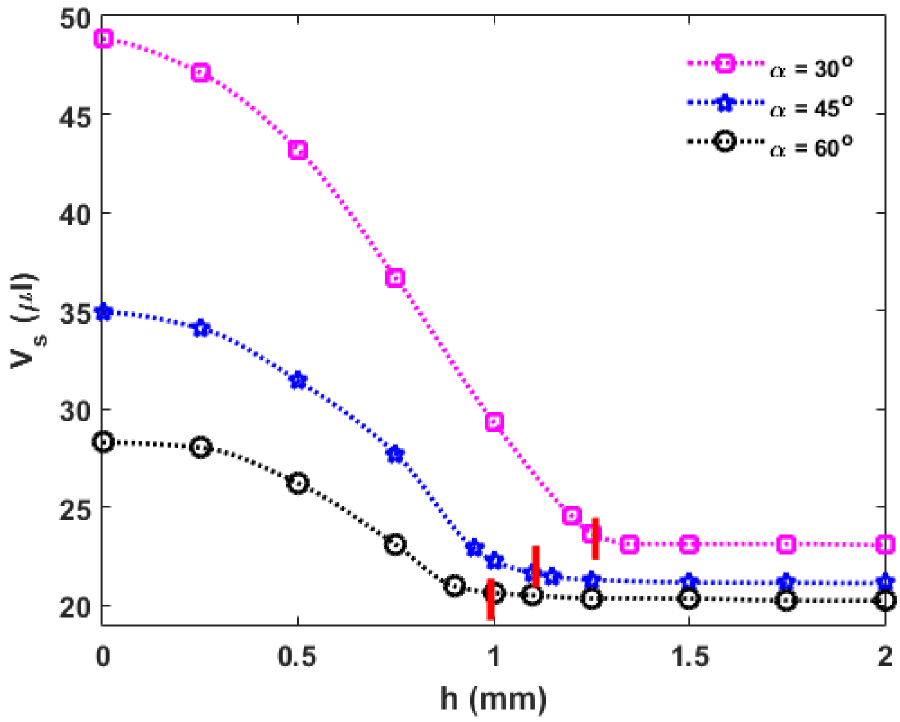

Fig.12. Variation of droplet shedding volume against bump height for different surface inclinations. The red bars indicate the critical bump heights.

To invesitgate the effects of patch wettability, the shedding volume is calculated for four diffenent patch contact angles, i.e., θ_{patch} = 30°, 50°, 81°, and 101°. Bump diameter and surface inclination are fixed at d = 2 mm and α = 45°, respectively. It is be seen from Fig. 13 that the shedding volume depeneds very much on the patch wettability. The surface with larger patch contact angle is able to dislodge the droplet with smaller volumes. Moreover, the critical bump height also reduces with the contact angle.

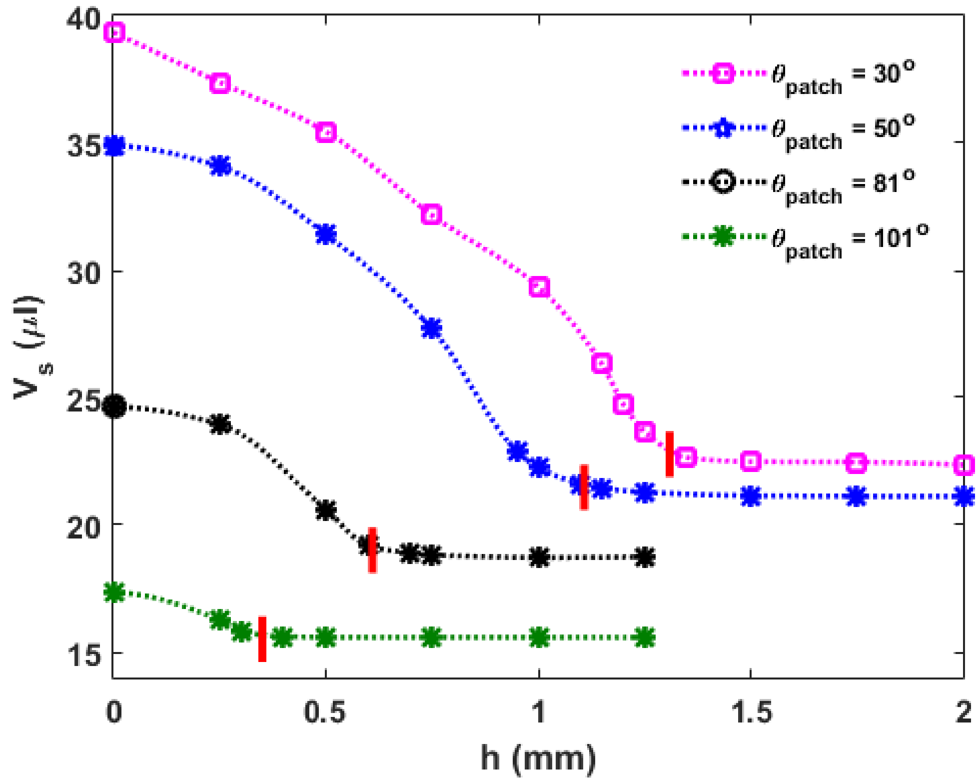

Fig.13. Variation of droplet shedding volume against bump height for different patch contact angles. The red bars indicate the critical bump heights.

4.3 Effects of bump scale

Efficient water collection requires two conditions: high condensation rate and effective removal of condensing droplets from the surface. The latter condition is very important as the removal of condensing droplets creates space for new droplets. In this section, the influence of bump scale on the droplet removal is investigated with two cylindrical bumps, one at micrometer scale and the other at millimeter scale. The micro-scale bump has a diameter of d =200 µm and a height of h = 500 µm, whereas the milli-scale bump has a diameter of d = 1 mm and a height of h = 2.5 mm. The aspect ratios of both bumps are the same, that is h/d = 1/2.5. Note the heights of both bumps are higher than their respective critical bump heights. In this section, a conversion factor 1.0 lu = 20.0 µm (see Table. 1.) is used from the lattice length unit to the physical length unit.

Figure 14 shows snapshots of droplet evolution on both bumps. It is seen that the droplet on the micro-scale bump assumes nearly spherical shape at all instants. This is because during the evolution its size remains smaller than the capillary length (about 2.7 mm), so that the surface tension force dominates over the gravitational force. Due to much smaller bump diameter droplet sheds quickly at t = 18000 (Fig. 14 (a2)). After the shedding, the droplet does not immediately move away from the bump. Instead, it stays at its new location until it grows big enough to enable the removal through large gravitational pull. This is evidenced in Fig. 14(a3) where the droplet cannot move far away from the bump from the droplet shedding time (t = 18000) to a much later time t = 36500. This inefficient removal may deteriorate the performance of water collection and cause problems such as water flooding of micro-structures. On the other hand, for the milli-scale bump, the droplet size of shedding droplet is comparable to the capillary length at shedding time t = 67700 (Fig. 14(b3)), so that the gravity can play an important role in the droplet removal from the surface. The droplet removal is much faster on the milli-scale bump, as revealed in Fig. 14(b4) to 14(b6). Hence, droplet shedding is faster for miro-scale bumps but the subsequent gravity assisted removal from surface is faster for mili-scale bump. To focus the discussion on the beetle bumps, in this paper droplet shedding only from milli-scale cylindrical bumps is investigated.

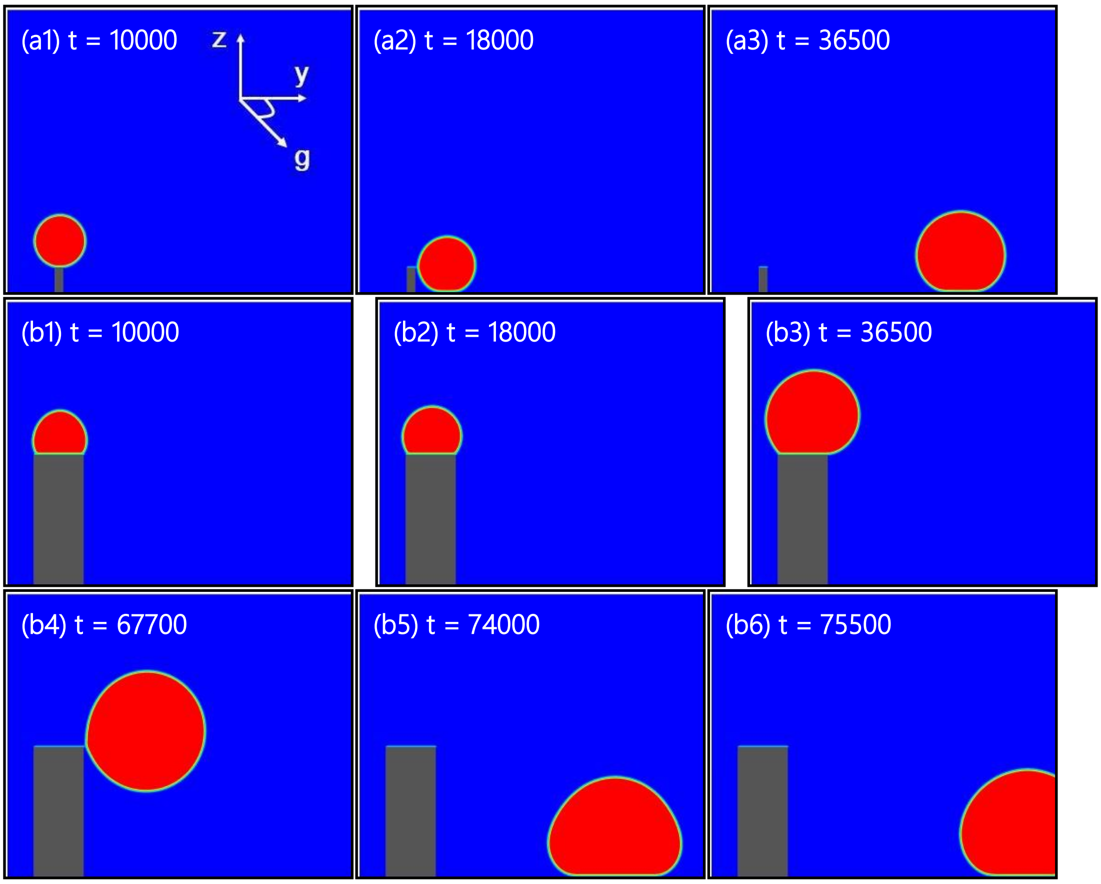

Fig.14. Droplet shedding and subsequent gravity-assisted removal from surfaces with bump dimensions (a) *d* = 200μm and *h* = 500μm (b) *d* = 1mm and *h* = 2.5 mm.

4.4 Scaling law

If one plots the normalized critical bump height h_c/d obtained from the above studies against a quantity $(\lambda/d)\cos\theta\cos\alpha$ that combines the capillary length λ, the hydrophilic wettability θ_{patch} and the surface inclination α, a linear relationship with an average error of 4% is found, as shown in Fig. 15. Curve fitting gives the following formula

$$\frac{h_c}{d} = \frac{\lambda}{d} 0.46 \cos\theta_{patch} \cos\alpha + 0.25 \quad (6)$$

Note the capillary length $\lambda = (\sigma/\rho g)^{1/2}$, where σ is the surface tension.

As revealed in previous sections, the droplet shedding volume decreases with the bump height till the critical bump height is achieved. It is also seen from Figs. 7 and 9 that the droplet shedding time reduces with the bump height, which will most likely reach a limit when the critical bump height is achieved. Since the water collection rate is proportional to the ratio of droplet shedding volume to shedding time, the increase of the bump height results in two counteracting factors that significantly affect the water collection. The present scaling law (i.e., Eq. (6)) provides a good prediction in the critical bump height, beyond which the droplet shedding time and shedding volume both reach their respective minimums, resulting in an unchanged water collection rate. In this sense, this scaling law can provide some guidance on the design of beetle-inspired bumps for water collection.

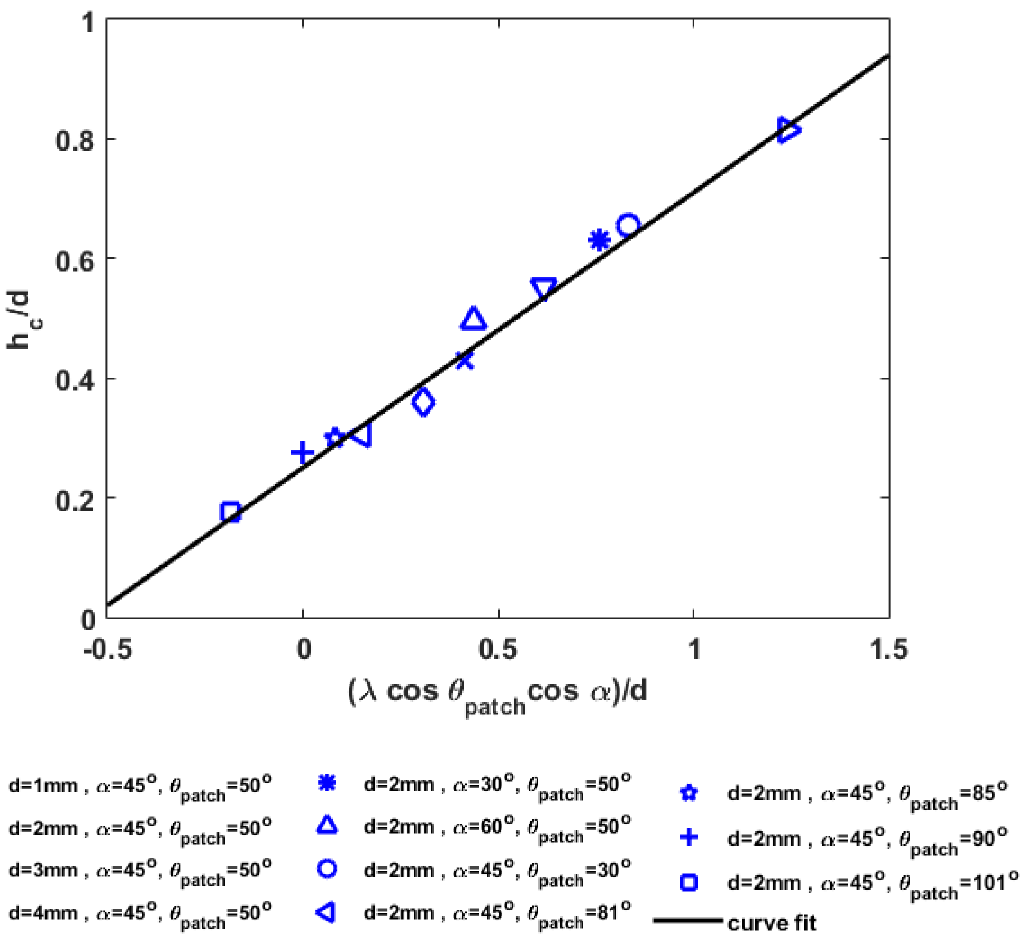

Fig.11. Curve fit relationship between the critical bump height and a combination of other parameters.

5. Conclusions

In this work, droplet shedding from desert beetle inspired bumps was numerically investigated using the lattice Boltzmann method. It was revealed that the bump shape and height can significantly influence the shedding volume of shedding droplets. The tangential component of gravity was observed to play an important role in early droplet shedding from bumps. The major findings of this work are summarized as follows:

1. The droplet shedding volume decreases with the bump height till the critical bump height is achieved.
2. The droplet shedding time reduces with the bump height, which will most likely reach a limit when the critical bump height is achieved.
3. With the same hydrophilic patch area, the droplet shedding volume is smaller on hemispherical bumps compared to on cylindrical bumps, due to their different surface curvatures.
4. Micro-scale bumps shed droplets smaller than the water capillary length, making the gravity-assisted droplet removal inefficient compared to milli-scale bumps.
5. For cylindrical bumps, the critical bump height increases with bump diameter, but decreases with the patch contact angle and surface inclination. Similar trends were also found for the droplet shedding volume.

Based on the simulation results, a scaling law (i.e., Eq. (6)) was proposed to estimate the critical bump height for cylindrical bumps based on bump geometrical conditions and patch wettability. This scaling law can provide some guidance on the design of beetle-inspired bumps for water collection.

Acknowledgement

SA would like to acknowledge the financial support from The Hong Kong Polytechnic University for his PhD study.

References

[1] N. Buras, Hydrology and Water Supply, in: Manag. Urban Water Supply, Springer Netherlands, Dordrecht, 2003: pp. 11–22. doi:10.1007/978-94-017-0237-9_2.

[2] S. Gorjian, B. Ghobadian, T. Tavakkoli Hashjin, A. Banakar, Experimental performance evaluation of a stand-alone point-focus parabolic solar still, Desalination. 352 (2014) 1–17. doi:10.1016/j.desal.2014.08.005.

[3] J.K. Domen, W.T. Stringfellow, M. Kay, C. Shelly, Fog water as an alternative and sustainable water resource, Clean Techn Env. Policy. 16 (2014) 235–249. doi:10.1007/s10098-013-0645-z.

[4] A.R. Parker, C.R. Lawrence, Water capture by a desert beetle, Nature. 414 (2001) 33–34. doi:10.1038/35102108.

[5] Y. Hou, M. Yu, X. Chen, Z. Wang, S. Yao, Recurrent filmwise and dropwise condensation on a beetle mimetic, 9 (2014) 71–81.

[6] L. Zhang, J. Wu, M.N. Hedhili, X. Yang, P. Wang, Inkjet printing for direct micropatterning of a superhydrophobic surface: toward biomimetic fog harvesting surfaces, J. Mater. Chem. A. 3 (2015) 2844–2852. doi:10.1039/C4TA05862C.

[7] K. Yin, H. Du, X. Dong, C. Wang, J. Duan, J. He, A simple way to achieve bioinspired hybrid wettability surface with micro/nanopatterns for efficient fog collection, Nanoscale. (2017). doi:10.1039/C7NR05683D.

[8] H. Bai, L. Wang, J. Ju, R. Sun, Y. Zheng, L. Jiang, Efficient water collection on integrative bioinspired surfaces with star-shaped wettability patterns, Adv. Mater. 26 (2014) 5025–5030. doi:10.1002/adma.201400262.

[9] K.C. Park, S.S. Chhatre, S. Srinivasan, R.E. Cohen, G.H. McKinley, Optimal Design of Permeable Fiber Network Structures for Fog Harvesting, Langmuir. 29 (2013) 13269–13277. doi:10.1021/la402409f.

[10] J.K. Park, S. Kim, Three-Dimensionally Structured Flexible Fog Harvesting Surfaces Inspired by Namib Desert Beetles, (2019). doi:10.3390/mi10030201.

[11] S.J. Hong, C.C. Chang, T.H. Chou, Y.J. Sheng, H.K. Tsao, A drop pinned by a designed patch on a tilted superhydrophobic surface: Mimicking desert beetle, J. Phys. Chem. C. 116 (2012) 26487–26495. doi:10.1021/jp310482y.

[12] C. Dorrer, J. Rühe, Mimicking the stenocara beetle - Dewetting of drops from a patterned superhydrophobic surface, Langmuir. 24 (2008) 6154–6158. doi:10.1021/la800226e.

[13] R.P. Garrod, L.G. Harris, W.C.E. Schofield, J. Mcgettrick, L.J. Ward, D.O.H. Teare, J.P.S. Badyal, Mimicking a Stenocara Beetle ' s Back for Microcondensation Using Plasmachemical Patterned Superhydrophobic - Superhydrophilic Surfaces, Langmuir. 23 (2007) 689–693. doi:10.1021/la0610856.

[14] S. Chen, G.D. Doolen, Lattice Boltzmann Method for fluid flows, 30 (1998) 329–364. doi:10.1007/978-3-540-27982-2.

[15] X. He, G.D. Doolen, Thermodynamic foundations of kinetic theory and Lattice Boltzmann models for multiphase flows, in: J. Stat. Phys., 2002: pp. 309–328. doi:10.1023/A:1014527108336.

[16] X. Shan, H. Chen, Lattice Boltzmann model for simulating flows with multi phases and components, Phys. Rev. E. 47 (1993) 1815–1819. doi:10.1103/PhysRevE.47.1815.

[17] X. Shan, H. Chen, Simulation of nonideal gases and liquid-gas phase transitions by the lattice Boltzmann equation, Phys. Rev. E. 49 (1994) 2941–2948. doi:10.1103/PhysRevE.49.2941.

[18] P. Yuan, L. Schaefer, Equations of state in a lattice Boltzmann model, Phys. Fluids. 18 (2006). doi:10.1063/1.2187070.

[19] R. Benzi, L. Biferale, M. Sbragaglia, S. Succi, F. Toschi, Mesoscopic modeling of a two-phase flow in the presence of boundaries: The contact angle, Phys. Rev.

E - Stat. Nonlinear, Soft Matter Phys. 74 (2006) 1–14. doi:10.1103/PhysRevE.74.021509.

[20] Z. Deng, C. Zhang, C. Shen, J. Cao, Y. Chen, Self-propelled dropwise condensation on a gradient surface, Int. J. Heat Mass Transf. 114 (2017) 419–429. doi:10.1016/j.ijheatmasstransfer.2017.06.065.

[21] Q. Zhang, D. Sun, Y. Zhang, M. Zhu, Lattice Boltzmann modeling of droplet condensation on superhydrophobic nanoarrays, Langmuir. 30 (2014) 12559–12569. doi:10.1021/la502641y.

[22] A. Dupuis, J.M. Yeomans, Droplets on patterned substrates: Water off a beetle's back, Int. J. Numer. Methods Fluids. 50 (2006) 255–261. doi:10.1002/fld.1130.

[23] X. Fu, Z. Yao, P. Hao, Numerical simulation of condensation on structured surfaces, Langmuir. 30 (2014) 14048–14055. doi:10.1021/la503504r.

[24] C.G.L. Furmidge, Studies at phase interfaces. I. The sliding of liquid drops on solid surfaces and a theory for spray retention, J. Colloid Sci. 17 (1962) 309–324. doi:https://doi.org/10.1016/0095-8522(62)90011-9.

[25] M. Miwa, A. Nakajima, A. Fujishima, K. Hashimoto, T. Watanabe, Effects of the Surface Roughness on Sliding Angles of Water Droplets on Superhydrophobic Surfaces, Langmuir. 16 (2000) 5754–5760. doi:10.1021/la991660o.

[26] H. Huang, M. Sukop, X. Lu, Multiphase Lattice Boltzmann Methods: Theory and Application, Wiley, 2015. https://books.google.com.hk/books?id=cGn3CQAAQBAJ.

[27] M.E. Kutay, A.H. Aydilek, E. Masad, Laboratory validation of lattice Boltzmann method for modeling pore-scale flow in granular materials, Comput. Geotech. 33 (2006) 381–395. doi:10.1016/j.compgeo.2006.08.002.